Perturbation Theory of High-T_c Superconductivity in Iron Pnictides

Takuji NOMURA*

Synchrotron Radiation Research Center, Japan Atomic Energy Agency, Sayo, Hyogo 679-5148

JST, TRIP, Sanbancho, Chiyoda, Tokyo 102-0075

The high-transition-temperature (high-T_c) superconductivity discovered recently in iron pnictides is analyzed within a perturbation theory. Specifically, the probable pairing symmetry, the doping dependence of the transition temperature and the pairing mechanism are studied by solving the Eliashberg equation for multi-band (2- and 5-band) Hubbard models with realistic electronic structures. The effective pairing interaction is expanded perturbatively in the on-site Coulomb integrals up to third order. Our perturbative weak-coupling approach shows that sufficiently large eigenvalues of the Eliashberg equation are obtained to explain the actual high transition temperatures by taking realistic on-site Coulomb integrals in the 5-band model. Thus, unconventional (non-phonon-mediated) superconductivity is highly likely to be realized. The superconducting order parameter does not change its sign on the Fermi surfaces, but it does change between the electron and hole Fermi surfaces. Consequently, the probable pairing symmetry is always "a nodeless extended s-wave symmetry (more specifically, an $s_\pm$-wave symmetry)" over the whole parameter region that we investigated. It is suggested that the 2-band model is insufficient to explain the high values of T_c.

1. Introduction

The recent discovery of high-T_c superconductivity in iron pnictides and related compounds has strongly intensified the research activity in solid-state physics. The highest transition temperature attained in iron pnictides is about 56 K to date, which is currently the highest reported superconducting transition temperature among noncuprate superconductors.

A prototypical iron-pnictide superconductor LaFeAsO$_{1-x}$F$_x$ (x =0.05-0.12, T_c = 26 K) was discovered by Kamihara et al.[1] Before the discovery of the arsenic superconducting system LaFeAsO$_{1-x}$F$_x$, it had been discovered that LaFePO$_{1-x}$F$_x$, where As in the arsenic system is replaced by P, is also a superconductor with T_c =3.2-6 K.[2] The LaFeAsO$_{1-x}$F$_x$ crystals are formed by stacking LaOF and FeAs layers alternately. Each iron atom is surrounded tetrahedrally by four As atoms, and each FeAs layer is constructed by connecting

---

*E-mail address: nomurat@spring8.or.jp

the edges of the As tetrahedra. In the undoped case $x = 0$, LaFeAsO appears to be a poor metal, and undergoes a structural transition from tetragonal to orthorhombic at 155 K and spin-density-wave (SDW) ordering below 137 K (with a wave vector $\boldsymbol{q} = (\pi, \pi, \pi)$ and a magnetic moment about 0.3-0.4μ_B on each iron atom at 0 K).[3] By substituting oxygen with fluorine, doped electrons cause metallic conduction with the disappearance of both the SDW and structural transitions for $x > 0.05$, and superconductivity occurs below about 26 K.[1] Moreover, subsequent studies clarified that replacement of La by other rare earth elements increases the transition temperature markedly: 41 K for Ce,[4] 52 K for Pr,[5] 52 K for Nd,[6] and 55 K for Sm.[7,8] Superconductivity has also been discovered in fluorine-free systems, including RFeAsO$_{1-y}$ (R=La, Ce, Pr, Nd, Sm, Gd. T_c = 31-55 K),[9–12] Gd$_{1-x}$Th$_x$FeAsO (T_c =56 K).[13] Hole-doped La$_{1-x}$Sr$_x$FeAsO also shows superconductivity with T_c =25 K.[14] Thus, a superconducting phase exists not only in the electron-doped side but also in the hole-doped side, and it appears that the superconducting transition is inhibited due to the structural distortion and SDW ordering only near the undoped case $x = 0$. It is natural to expect that superconductivity in all of these compounds occurs basically by the same mechanism, in spite of the quantitative difference in T_c.

In addition to RFeAsO$_{1-x}$F$_x$ (R: rare-earth element) series, many other related superconducting iron compounds without oxygen have been discovered, e.g., Ba$_{1-x}$K$_x$Fe$_2$As$_2$ (T_c =38 K),[15] Li$_{1-x}$FeAs (T_c = 18 K),[16,17] and Ca$_{1-x}$Na$_x$Fe$_2$As$_2$ (T_c =20 K).[18] In these related compounds, FeAs layers are separated not by layers of rare-earth elements and oxygen, but by layers of BaK, Li, or other various elements. Therefore, we naturally consider that the feature essential for the superconductivity is the existence of FeAs layers, while the remaining elements may play only a relatively minor role of a carrier reservoir or spacing between the FeAs layers. In fact, similar superconductivity has also been observed in α-FeSe (T_c =8 K),[19] in which the valence number of the iron atoms may be the same as that in iron pnictides but no spacing elements are inserted between the FeSe layers. This fact suggests that only the layers of square networks constructed from iron atoms may be necessary for superconductivity.

Electronic structure calculations for some of the above-mentioned iron-based superconductors have already been carried out in many studies.[20–26] According to these studies, the electronic states near the Fermi level are formed dominantly by the Fe3d electronic states. Thus, iron pnictides may be considered to be typical strongly correlated electron systems, in which the strong Coulomb interaction among the iron 3d electrons can affect the electronic properties significantly. The Fermi surface consists of hole pockets around the Γ point and electron pockets around the M point, qualitatively consistent with the results of angle-resolved photoemission (ARPES) experiments[27–29] and more recent quantum oscillation experiments.[30]

An important step toward understanding this newly discovered iron-pnictide superconductivity will be to clarify whether it is conventional phonon-mediated superconductivity or

unconventional superconductivity such as that in copper oxides. There are already several reasons why unconventional pairing may be realized in iron pnictides: (i) T_c is very high, compared with conventional phonon-mediated BCS superconductors, (ii) Fe3d states dominate the majority of the density of states near the Fermi level,[21, 22] as mentioned above, and therefore the electron correlation originating from the Coulomb interaction on the relatively localized Fe3d bands is considered to be strong in these systems, and (iii) electron-phonon coupling is expected to be weak according to first-principles calculations.[22] Thus, it will be a very interesting issue to determine whether or not we can understand iron-pnictide superconductivity as a natural result of electron correlations, as in the case of unconventional superconductivity in many other strongly correlated systems.

So many theoretical works on iron-pnictide superconductivity have already been presented that we cannot review all of them here. Many of them focus on the pairing mechanism and pairing symmetry. Among the proposed pairing symmetries, the most promising pairing symmetry is a spin-singlet extended s-wave ($s_\pm$-wave) symmetry, in which the superconducting order parameter changes its sign between the Fermi surfaces. This pairing symmetry has been suggested in considerations based on the magnetic susceptibility,[31] random-phase approximation (RPA),[23, 32] renormalization group (RG) calculations,[33, 34] fluctuation-exchange approximation (FLEX)[35] and other studies.[36] The $s_\pm$-wave pairing symmetry appears now to be consistent with the results of most experiments, including those based on ARPES,[27, 28] penetration depth,[37] and neutron scattering.[38] A recent theoretical study suggests that the sign reversal of the $s_\pm$-wave pairing symmetry is consistent also with nonmagnetic impurity effects.[39] Further investigations are still desirable to confirm that this pairing symmetry is indeed realized in iron-pnictide superconductors. Our present theoretical study will provide additional support for this pairing symmetry.

In the present work we present a microscopic theory of iron-pnictide superconductivity. We take a weak-coupling approach on the basis of third-order perturbation theory with respect to the electron Coulomb interaction among the Fe3d electrons. This perturbative approach has been applied to many realistic electronic structures in order to discuss the pairing symmetry and pairing mechanism in real strongly correlated electron systems, and has succeeded in explaining various exotic pairing states, including the $d_{x^2-y^2}$-wave states in cuprate and organic superconductors,[40–42] the triplet p-wave state in Sr_2RuO_4,[43, 44] the $d_{x^2-y^2}$-wave states in several heavy-fermion superconductors.[45–47] Therefore, it is interesting to also apply this approach to iron-pnictide superconductors. Specifically, the probable pairing symmetry, the momentum and band dependences of the superconducting order parameter, the doping dependence of the transition temperature, and the pairing mechanism are investigated by solving the Eliashberg equation for 2- and 5-band Hubbard models with realistic electronic structures. The effective pairing interaction is expanded perturbatively in the on-site Coulomb

integrals up to third order. Our weak-coupling approach shows that sufficiently high values of T_c are obtained for realistic values of the on-site Coulomb interaction in the 5-band models in order to explain the experimentally observed high values of T_c. Thus, it is concluded that unconventional (non-phonon-mediated) pairing is highly likely to be realized in iron-pnictide superconductivity. The superconducting order parameter does not change its sign on the Fermi surfaces without any nodes, but it does change between the electron and hole Fermi pockets. Consequently, the probable pairing symmetry is a spin-singlet extended s-wave or, more specifically, an $s_\pm$-wave symmetry. The calculated transition temperatures do not depend so sensitively on doping concentration, consistent with the results of experiments, but should drop suddenly around doping levels where some electron or hole pockets disappear. This suggests that nesting between the electron and hole Fermi pockets is responsible for this unconventional pairing. It is suggested that the 2-band model is insufficient to explain the high transition temperatures. The present article is a detailed version of our previous short article.[48]

2. Formulation

In the present work, we use multi-band tight-binding models to describe the electronic structure near the Fermi level. Taking account of the two-dimensionality of the actual crystal and electronic structure, we use two-dimensional tight-binding models. The unit cell in a single FeAs layer contains two iron atoms. Here we should note that the electronic structure near the Fermi level is dominated by the Fe3d orbitals, as many electronic structure calculations demonstrate, and will be reproduced effectively by taking only the Fe3d-like local orbitals (or more specifically, maximally localized Wannier orbitals, as presented in ref. 49). As Kuroki et al. pointed out,[23] by extracting only Fe3d-like states, we can effectively construct a tight-binding model on a simple two-dimensional square lattice consisting of only iron sites. This simplified scheme helps us greatly by reducing the number of energy bands to be considered. Thus, the noninteracting part of the Hamiltonian is expressed as follows:

$$H_0 = \sum_{i,j} \sum_{\ell,\ell'} \sum_{\sigma} t_{i\ell,j\ell'} c_{i\ell\sigma}^{\dagger} c_{j\ell'\sigma}, \tag{1}$$

where i and j denote iron sites on the square lattice, $\ell(\ell')$ denote Fe3d-like localized orbitals, and $c_{i\ell\sigma}$ ($c_{i\ell\sigma}^{\dagger}$) is the annihilation (creation) operator of electrons of Fe3d-like orbital ℓ at site i with spin σ. Here note again that the index specifying each of the two iron atoms in a unit cell is not necessary. Specific choices of $t_{i\ell,j\ell'}$ are given in §3.1 and §4.1.

We can diagonalize H_0 by using a unitary transformation in the form

$$H_0 = \sum_{\boldsymbol{k}} \sum_{a} \sum_{\sigma} E_a(\boldsymbol{k}) c_{\boldsymbol{k}a\sigma}^{\dagger} c_{\boldsymbol{k}a\sigma}, \tag{2}$$

where the index a specifies each of the diagonalized bands and $\boldsymbol{k}$ is momentum. $E_a(\boldsymbol{k})$ is the

diagonalized-band energy, and $c_{\boldsymbol{k}a\sigma}$ is related to $c_{i\ell\sigma}$ by

$$c_{i\ell\sigma} = \frac{1}{\sqrt{N}} \sum_{\boldsymbol{k}} \sum_{a} U_{\ell a}(\boldsymbol{k}) e^{\mathrm{i}\boldsymbol{k}\cdot\boldsymbol{r}_i} c_{\boldsymbol{k}a\sigma}, \tag{3}$$

where N is the number of iron lattice sites and $U_{\ell a}(\boldsymbol{k})$ represents the elements of the diagonalization matrix.

The electrons on the local orbitals will be affected by the on-site Coulomb interaction. The interacting part is given in the following form:

$$
\begin{aligned}
H' &= \frac{U}{2} \sum_{i} \sum_{\ell} \sum_{\sigma\neq\sigma'} c^{\dagger}_{i\ell\sigma} c^{\dagger}_{i\ell\sigma'} c_{i\ell\sigma'} c_{i\ell\sigma} + \frac{U'}{2} \sum_{i} \sum_{\ell\neq\ell'} \sum_{\sigma,\sigma'} c^{\dagger}_{i\ell\sigma} c^{\dagger}_{i\ell'\sigma'} c_{i\ell'\sigma'} c_{i\ell\sigma} \\
&+ \frac{J}{2} \sum_{i} \sum_{\ell\neq\ell'} \sum_{\sigma,\sigma'} c^{\dagger}_{i\ell\sigma} c^{\dagger}_{i\ell'\sigma'} c_{i\ell\sigma'} c_{i\ell'\sigma} + \frac{J'}{2} \sum_{i} \sum_{\ell\neq\ell'} \sum_{\sigma\neq\sigma'} c^{\dagger}_{i\ell\sigma} c^{\dagger}_{i\ell\sigma'} c_{i\ell'\sigma'} c_{i\ell'\sigma},
\end{aligned}
\tag{4}
$$

where U, U', J, and J' are the Coulomb integrals for the intraorbital Coulomb interaction, the interorbital Coulomb interaction, the Hund's coupling, and the interorbital pair transfers, respectively. The total Hamiltonian is given by

$$H = H_0 + H'. \tag{5}$$

Propagation of the electrons of band a in the normal state is described by the normal Green's function:

$$G_a^{(0)}(k) = \frac{1}{\mathrm{i}\omega_n - E_a(\boldsymbol{k})}, \tag{6}$$

where $k = (\boldsymbol{k}, \mathrm{i}\omega_n)$ and ω_n is the fermionic Matsubara frequency: $\omega_n = (2n+1)\pi T$. Superconducting transition points can be determined by the linearized Eliashberg equation:

$$\Delta_{a\sigma_1\sigma_2}(k) = -\frac{T}{N} \sum_{k'} \sum_{a'} \sum_{\sigma_3\sigma_4} V_{a\sigma_1\sigma_2, a'\sigma_4\sigma_3}(k, k') |G_{a'}^{(0)}(k')|^2 \Delta_{a'\sigma_3\sigma_4}(k'), \tag{7}$$

where σ_i are spin indices, T is temperature, $\Delta_{a\sigma_1\sigma_2}(k)$ is the anomalous self-energy on band a, and $V_{a\sigma_1\sigma_2, a'\sigma_3\sigma_4}(k, k')$ is the effective pairing interaction. We have used the shorthand notation $\sum_k = \sum_{\boldsymbol{k}} \sum_{\omega_n}$. At superconducting transition points, the Eliashberg equation has a non-self-evident solution, i.e., $\Delta_{a\sigma\sigma'}(k) \not\equiv 0$. Replacing the left-hand side of eq. (7) by $\lambda\Delta_{a\sigma_1\sigma_2}(k)$, then eq. (7) is regarded as an eigenvalue equation with the eigenvalue λ and eigenfunction $\Delta_{a\sigma_1\sigma_2}(k)$, and transition points are determined by the condition $\lambda_{\max} = 1$, where $\lambda_{\max}$ is the maximum eigenvalue. Since $\lambda_{\max}$ is usually a monotonically decreasing function of T, therefore the superconducting instability is already attained for $\lambda_{\max} > 1$ and normal state is still favored for $\lambda_{\max} < 1$. The momentum dependence and spin symmetry of the eigenfunction $\Delta_{a\sigma_1\sigma_2}(k)$ giving $\lambda_{\max}$ characterize the most favorable pairing state.

Evaluation of the effective pairing interaction $V_{a\sigma_1\sigma_2, a'\sigma_3\sigma_4}(k, k')$ is a quantum many-body problem. The pairing interaction is expressed in the orbital representation by using the diag-

onalization matrix elements $U_{\ell a}(\boldsymbol{k})$ as follows:

$$V_{a\sigma_1\sigma_2,a'\sigma_3\sigma_4}(k,k') = \sum_{\{\ell_n\}} U^*_{\ell_1 a}(\boldsymbol{k})U^*_{\ell_2 a}(-\boldsymbol{k})V_{\zeta_1\zeta_2,\zeta_3\zeta_4}(k,k')U_{\ell_3 a'}(-\boldsymbol{k}')U_{\ell_4 a'}(\boldsymbol{k}'), \tag{8}$$

where ζ_n is the orbital-spin combined index, i.e., $\zeta_n = (\ell_n, \sigma_n)$, $U^*_{\ell a}(\boldsymbol{k})$ is the complex conjugate of $U_{\ell a}(\boldsymbol{k})$, and the summation with $\{\ell_n\}$ denotes that with respect to all of ℓ_1, ℓ_2, ℓ_3, and ℓ_4. Here we define the Green's function in the orbital representation by

$$G^{(0)}_{\zeta_1\zeta_2}(k) = \sum_a U_{\ell_1 a}(\boldsymbol{k})U^*_{\ell_2 a}(\boldsymbol{k})G^{(0)}_a(k)\delta_{\sigma_1\sigma_2}. \tag{9}$$

We note that H' can be expressed in the form

$$H' = \frac{1}{2}\sum_i \sum_{\{\zeta_n\}} I_{\zeta_1\zeta_2,\zeta_3\zeta_4} c^\dagger_{i\ell_1\sigma_1} c^\dagger_{i\ell_2\sigma_2} c_{i\ell_3\sigma_3} c_{i\ell_4\sigma_4}, \tag{10}$$

with

$$\left.\begin{array}{rcl} I_{(\ell\sigma)(\ell\bar{\sigma}),(\ell\bar{\sigma})(\ell\sigma)} & = & U \\ I_{(\ell\sigma)(\ell'\sigma),(\ell'\sigma)(\ell\sigma)} & = & U' - J \\ I_{(\ell\sigma)(\ell'\bar{\sigma}),(\ell'\bar{\sigma})(\ell\sigma)} & = & U' \\ I_{(\ell\sigma)(\ell'\bar{\sigma}),(\ell\bar{\sigma})(\ell'\sigma)} & = & J \\ I_{(\ell\sigma)(\ell\bar{\sigma}),(\ell'\bar{\sigma})(\ell'\sigma)} & = & J' \end{array}\right\}, \tag{11}$$

and the other elements are zero, where $\ell \neq \ell'$ and $\sigma \neq \bar{\sigma}$. The summation with $\{\zeta_n\}$ denotes that with respect to all of the orbital and spin indices, ℓ_n and σ_n. It is useful to define the antisymmetrized bare Coulomb vertex by

$$\Gamma^{(0)}_{\zeta_1\zeta_2,\zeta_3\zeta_4} = I_{\zeta_1\zeta_2,\zeta_3\zeta_4} - I_{\zeta_1\zeta_2,\zeta_4\zeta_3}. \tag{12}$$

We expand $V_{\zeta_1\zeta_2,\zeta_3\zeta_4}(k,k')$ perturbatively to third order in H', using $G^{(0)}_{\zeta_1\zeta_2}(k)$ and $\Gamma^{(0)}_{\zeta_1\zeta_2,\zeta_3\zeta_4}$. Diagrammatic representations of the perturbation terms are displayed in Fig. 1. The Eliashberg equation in the orbital representation is written using the anomalous Green's function $F_{\zeta_1\zeta_2}(k)$ as

$$\Delta_{\zeta_1\zeta_2}(k) = -\frac{T}{N}\sum_{k'}\sum_{\zeta_3\zeta_4} F_{\zeta_3\zeta_4}(k')V_{\zeta_1\zeta_2,\zeta_4\zeta_3}(k,k'). \tag{13}$$

Through the expansion of $V_{\zeta_1\zeta_2,\zeta_4\zeta_3}(k,k')$, the anomalous self-energy $\Delta_{\zeta_1\zeta_2}(k)$ is also expanded as

$$\begin{array}{rcl} \Delta_{\zeta_1\zeta_2}(k) & = & \Delta^{(1)}_{\zeta_1\zeta_2}(k) + \Delta^{(2)}_{\zeta_1\zeta_2}(k) + \Delta^{(3-1)}_{\zeta_1\zeta_2}(k) \\ & & +\Delta^{(3-2)}_{\zeta_1\zeta_2}(k) + \Delta^{(3-2*)}_{\zeta_1\zeta_2}(k) + \Delta^{(3-3)}_{\zeta_1\zeta_2}(k) + \Delta^{(3-3*)}_{\zeta_1\zeta_2}(k). \end{array} \tag{14}$$

The analytic expressions of the contributions are

$$\Delta^{(1)}_{\zeta_1\zeta_2}(k) = -\frac{1}{2}\frac{T}{N}\sum_{k'}\sum_{\zeta_3\zeta_4} F_{\zeta_3\zeta_4}(k')\Gamma^{(0)}_{\zeta_1\zeta_2,\zeta_4\zeta_3}, \tag{15}$$
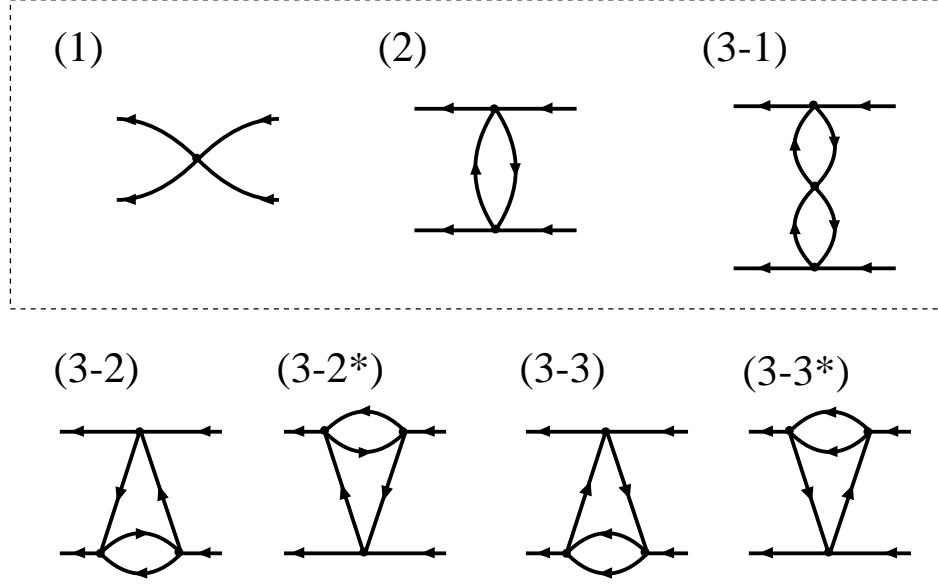
Fig. 1. Diagrammatic representation of the effective pairing interaction $V_{\zeta_1\zeta_2,\zeta_3\zeta_4}(k, k')$ in the third-order perturbation theory. Each vertex and solid line with an arrowhead represent the on-site Coulomb interaction $\Gamma^{(0)}_{\zeta_1\zeta_2,\zeta_3\zeta_4}$ and the Green's function $G^{(0)}_{\zeta_1\zeta_2}(k)$, respectively. The contributions enclosed by the broken rectangle, (1), (2), and (3-1), are also included in RPA calculations, while the remaining contributions, (3-2), (3-2*), (3-3), and (3-3*) are the vertex corrections and are not included within the RPA.

$$\Delta^{(2)}_{\zeta_1\zeta_2}(k) = \frac{T}{N}\sum_{k'}\sum_{\zeta_3\zeta_4}\sum_{\{\gamma_n\}}F_{\zeta_3\zeta_4}(k')\chi^{(0)}_{\gamma_4\gamma_2,\gamma_1\gamma_3}(k-k')\Gamma^{(0)}_{\zeta_1\gamma_4,\gamma_2\zeta_3}\Gamma^{(0)}_{\gamma_1\zeta_2,\zeta_4\gamma_3}, \tag{16}$$

$$\Delta^{(3-1)}_{\zeta_1\zeta_2}(k) = -\frac{T}{N}\sum_{k'}\sum_{\zeta_3\zeta_4}\sum_{\{\gamma_n\}}\sum_{\{\xi_n\}}F_{\zeta_3\zeta_4}(k')\chi^{(0)}_{\gamma_4\gamma_2,\gamma_1\gamma_3}(k-k')\chi^{(0)}_{\xi_4\xi_2,\xi_1\xi_3}(k-k')$$
$$\times\Gamma^{(0)}_{\zeta_1\gamma_4,\gamma_2\zeta_3}\Gamma^{(0)}_{\gamma_1\xi_4,\xi_2\gamma_3}\Gamma^{(0)}_{\xi_1\zeta_2,\zeta_4\xi_3}, \tag{17}$$

$$\Delta^{(3-2)}_{\zeta_1\zeta_2}(k) = -\left(\frac{T}{N}\right)^2\sum_{k'k_1}\sum_{\zeta_3\zeta_4}\sum_{\{\gamma_n\}}\sum_{\{\xi_n\}}F_{\zeta_3\zeta_4}(k')G^{(0)}_{\gamma_2\gamma_1}(k-k'+k_1)\chi^{(0)}_{\xi_4\xi_1,\xi_2\xi_3}(k+k_1)$$
$$\times G^{(0)}_{\gamma_3\gamma_4}(k_1)\Gamma^{(0)}_{\zeta_1\gamma_4,\gamma_2\zeta_3}\Gamma^{(0)}_{\gamma_1\xi_3,\xi_4\xi_2}\Gamma^{(0)}_{\xi_1\zeta_2,\xi_4\gamma_3}, \tag{18}$$

$$\Delta^{(3-2*)}_{\zeta_1\zeta_2}(k) = -\left(\frac{T}{N}\right)^2\sum_{k'k_1}\sum_{\zeta_3\zeta_4}\sum_{\{\gamma_n\}}\sum_{\{\xi_n\}}F_{\zeta_3\zeta_4}(k')G^{(0)}_{\gamma_1\gamma_2}(-k+k'+k_1)\chi^{(0)}_{\xi_3\xi_2,\xi_1\xi_4}(-k+k_1)$$
$$\times G^{(0)}_{\gamma_4\gamma_3}(k_1)\Gamma^{(0)}_{\zeta_1\xi_2,\gamma_4\xi_3}\Gamma^{(0)}_{\xi_4\gamma_2,\xi_1\zeta_3}\Gamma^{(0)}_{\gamma_3\zeta_2,\zeta_4\gamma_1}, \tag{19}$$

$$\Delta^{(3-3)}_{\zeta_1\zeta_2}(k) = -\frac{1}{2}\left(\frac{T}{N}\right)^2\sum_{k'k_1}\sum_{\zeta_3\zeta_4}\sum_{\{\gamma_n\}}\sum_{\{\xi_n\}}F_{\zeta_3\zeta_4}(k')G^{(0)}_{\gamma_1\gamma_2}(-k+k'+k_1)\phi^{(0)}_{\xi_1\xi_4,\xi_2\xi_3}(-k+k_1)$$
$$\times G^{(0)}_{\gamma_4\gamma_3}(k_1)\Gamma^{(0)}_{\zeta_1\gamma_2,\gamma_4\zeta_3}\Gamma^{(0)}_{\xi_3\xi_2,\zeta_4\gamma_1}\Gamma^{(0)}_{\gamma_3\zeta_2,\xi_1\xi_4}, \tag{20}$$

$$\Delta_{\zeta_1\zeta_2}^{(3-3*)}(k) = -\frac{1}{2}\left(\frac{T}{N}\right)^2 \sum_{k'k_1}\sum_{\zeta_3\zeta_4}\sum_{\{\gamma_n\}}\sum_{\{\xi_n\}} F_{\zeta_3\zeta_4}(k')G_{\gamma_2\gamma_1}^{(0)}(k-k'+k_1)\phi_{\xi_2\xi_3,\xi_1\xi_4}^{(0)}(k+k_1)$$

$$\times G_{\gamma_3\gamma_4}^{(0)}(k_1)\Gamma_{\zeta_1\gamma_4,\xi_3\xi_2}^{(0)}\Gamma_{\xi_1\xi_4,\gamma_2\zeta_3}^{(0)}\Gamma_{\gamma_1\zeta_2,\zeta_4\gamma_3}^{(0)}, \tag{21}$$

with

$$\chi_{\xi_1\xi_2,\xi_3\xi_4}^{(0)}(q) = -\frac{T}{N}\sum_k G_{\xi_4\xi_1}^{(0)}(k)G_{\xi_2\xi_3}^{(0)}(q+k), \tag{22}$$

$$\phi_{\xi_1\xi_2,\xi_3\xi_4}^{(0)}(q) = -\frac{T}{N}\sum_k G_{\xi_1\xi_3}^{(0)}(k)G_{\xi_2\xi_4}^{(0)}(q-k). \tag{23}$$

The factor of $\frac{1}{2}$ in eqs. (15), (20), and (21) is necessary to avoid double counting. The band indices are replaced with orbital indices by using the diagonalization matrix:

$$\Delta_{a\sigma_1\sigma_2}(k) = \sum_{\ell_1\ell_2} U_{\ell_1 a}^*(\boldsymbol{k})U_{\ell_2 a}^*(-\boldsymbol{k})\Delta_{\zeta_1\zeta_2}(k), \tag{24}$$

$$F_{\zeta_1\zeta_2}(k) = \sum_a U_{\ell_1 a}(\boldsymbol{k})U_{\ell_2 a}(-\boldsymbol{k})F_{a\sigma_1\sigma_2}(k). \tag{25}$$

The anomalous Green's function is related to the anomalous self-energy by

$$F_{a\sigma_1\sigma_2}(k) = |G_a^{(0)}(k)|^2\Delta_{a\sigma_1\sigma_2}(k) \tag{26}$$

in the band representation. Note that this relation is valid only in the region where the superconducting order parameter is nonzero but small (i.e., in the vicinity of transition points), since all quantities in the present formulation are linearized with respect to the anomalous functions. It is clear that eq. (7) can be consistently obtained from eqs. (13), (25), (26), (24), and (8). The anomalous functions $\Delta_{a\sigma_1\sigma_2}(k)$ and $F_{a\sigma_1\sigma_2}(k)$ can be determined by eqs. (7) and (26), which is carried out numerically. For numerical calculations in the present study, we take 32×32 $\boldsymbol{k}$-points in the first Brillouin zone and 512 Matsubara frequencies. The momentum and frequency summations are performed using the fast Fourier transformation.

We now turn our attention to the remaining degrees of freedom in the phase factor of the diagonalization matrix elements $U_{\ell a}(\boldsymbol{k})$. We can easily verify that if $U_{\ell a}(\boldsymbol{k})$ diagonalizes H_0, then $U_{\ell a}(\boldsymbol{k})e^{\mathrm{i}\phi_a(\boldsymbol{k})}$ also diagonalizes H_0, where $\phi_a(\boldsymbol{k})$ is an arbitrary real function of $\boldsymbol{k}$. It is easy to see that $G_{\zeta_1\zeta_2}^{(0)}(k)$ and $V_{\zeta_1\zeta_2,\zeta_3\zeta_4}(k,k')$ do not depend on the choice of phase function $\phi_a(\boldsymbol{k})$. However, the values of $V_{a\sigma_1\sigma_2,a'\sigma_3\sigma_4}(k,k')$ and the anomalous functions depend on $\phi_a(\boldsymbol{k})$ in general, since they are subject to extrinsic phase modulations. In order to avoid this unfavorable situation, it is natural to assume the following condition:

$$U_{\ell a}(\boldsymbol{k}) = U_{\ell a}^*(-\boldsymbol{k}). \tag{27}$$

We use this condition throughout the present work.

In the present formulation, we have taken only the diagonal components of anomalous functions with respect to band indices and have neglected the off-diagonal components. Here

note that the diagonal components describe intraband pairing, while the off-diagonal ones describe interband pairing. Superconducting instability is generally connected with the logarithmic increase in the pair-correlation function at low temperatures. While the diagonal pair correlations exhibit this increase down to zero temperature, the off-diagonal ones do not in general. This is because the increase of the pair correlations between different bands stops below a temperature comparable to the energy difference between the bands. Thus, we may neglect the off-diagonal components for the reliable prediction of pairing symmetry at low temperatures.

The same formulation presented here was previously applied to the spin-triplet superconductivity in Sr_2RuO_4 by the present author and Yamada.[44] In the present section we have given improved and more useful analytic expressions for the perturbation terms.

3. Analysis of 5-band Hubbard model

3.1 5-band tight-binding model by Kuroki et al.

In this section, we present an analysis based on a 5-band model. Following Kuroki et al,[23] we take the five local Fe3d-like orbitals: $\ell = 3Z^2 - R^2$, XZ, YZ, $X^2 - Y^2$, and XY. The tight-binding parameters $t_{i\ell,j\ell'}$ are provided in ref. 23. Here we should bear in mind that the original unit cell contains two iron atoms. The principal axes X and Y are taken along the basal plane parallel to the FeAs layers, and the Z-axis is taken to be perpendicular to the basal plane, with respect to this original unit cell. The above orbital states are represented using these original coordinates. Neglecting the As sites in the effective models, the remaining iron atoms form a two-dimensional square lattice in which each unit cell contains only one iron atom. The principal axes x and y with respect to this new unit cell are parallel to the nearest-neighbor iron-iron bonds and are obtained by rotating the original axes X and Y by $45°$ in the basal plane. In momentum space, the original Brillouin zone in which positions are parametrized by $\boldsymbol{k} = (k_X, k_Y)$ is extended to a wide Brillouin zone in which positions are parametrized by $\boldsymbol{k} = (k_x, k_y)$.

The electronic structure of the 5-band model is shown in Fig. 2. The total electron number n is related to the doping level x by $x = n - 6$. The Fermi surface for $x = 0.1$ forms five Fermi pockets in the extended Brillouin zone: two hole pockets (α and β) around $(0,0)$, one hole pocket (α') around (π, π), and electron pockets (γ and γ') around $(\pi, 0)$ and $(0, \pi)$. In the original folded representation, both $(0,0)$ and (π, π) in the extended Brillouin zone are folded onto the Γ point, and $(\pi, 0)$ and $(0, \pi)$ are folded onto the M point. Thus, three concentric hole-like surfaces will be located around the Γ point, and two concentric electron-like surfaces will be constructed around the M point, in the original folded Brillouin zone. The XZ, YZ, and $X^2 - Y^2$ states occupy most of the density of states near the Fermi level and are naturally expected to dominate the electronic properties including the superconductivity.
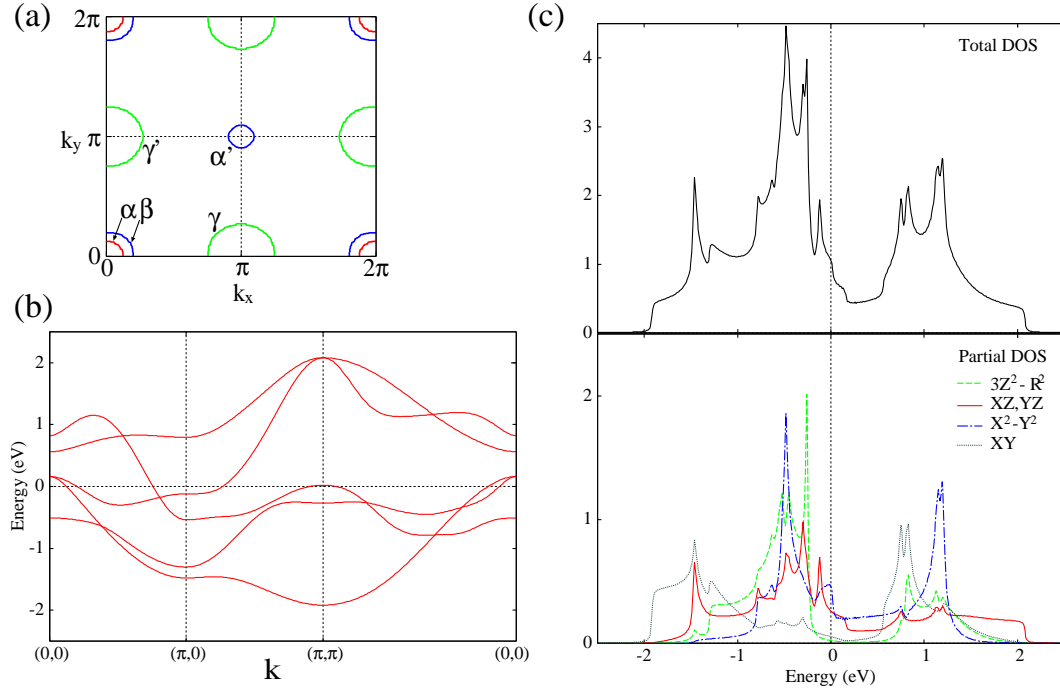
Fig. 2.   (Color online) Electronic structure of the 5-band model by Kuroki et al. in ref. 23. (a) Fermi surface and (b) energy band dispersion, both of which are depicted in the extended Brillouin zone. (c) total density of states and partial density of states for the orbitals, $3Z^2 - R^2$, XZ, YZ, $X^2 - Y^2$ and XY. The Fermi level is set to zero on the horizontal axis.

3.2   Favorable pairing symmetry

The most favorable pairing symmetry is obtained from the eigenfunction giving the maximum eigenvalues of the Eliashberg equation. In Fig. 3, the eigenvalues for various pairing symmetries at $x = 0.10$ are shown as a function of temperature. The most favorable pairing symmetry is the spin-singlet s-wave (or more appropriately, as we shall see below, the extended s-wave or $s_{\pm}$-wave), and the maximum eigenvalue is sufficiently large to explain the actual high transition temperatures for realistic values of the Coulomb interaction: $U = 1.2$ eV, $U' = 0.9$ eV, and $J = J' = 0.15$ eV. In Fig. 3, the transition temperature is evaluated to be about 100 K from the condition $\lambda_{\max}(T_c) = 1$.

We number the energy bands $E_a(\boldsymbol{k})$ ($a = 1, \cdots, 5$) in ascending order with respect to energy, i.e., $a < a'$ for $E_a(\boldsymbol{k}) < E_{a'}(\boldsymbol{k})$ at any $\boldsymbol{k}$. The three bands, $a = 2, 3$, and 4, cross the Fermi level. The momentum dependences of the anomalous Green's functions $F_a(k)$ at $\omega_n = \pi T$ on these three bands are displayed in Figs. 4(a)-(c). Here we have suppressed the spin part of the spin-singlet anomalous Green's functions by using the Pauli spin matrix σ_y: $F_{a\sigma_1\sigma_2}(k) = F_a(k)[i\sigma_y]_{\sigma_1\sigma_2}$. As we see in Fig. 4, the zero contours of the anomalous functions do not have any cross sections with the Fermi surfaces. Thus, we conclude that the superconducting gap will fully open on the Fermi surfaces, noting that the nodal positions
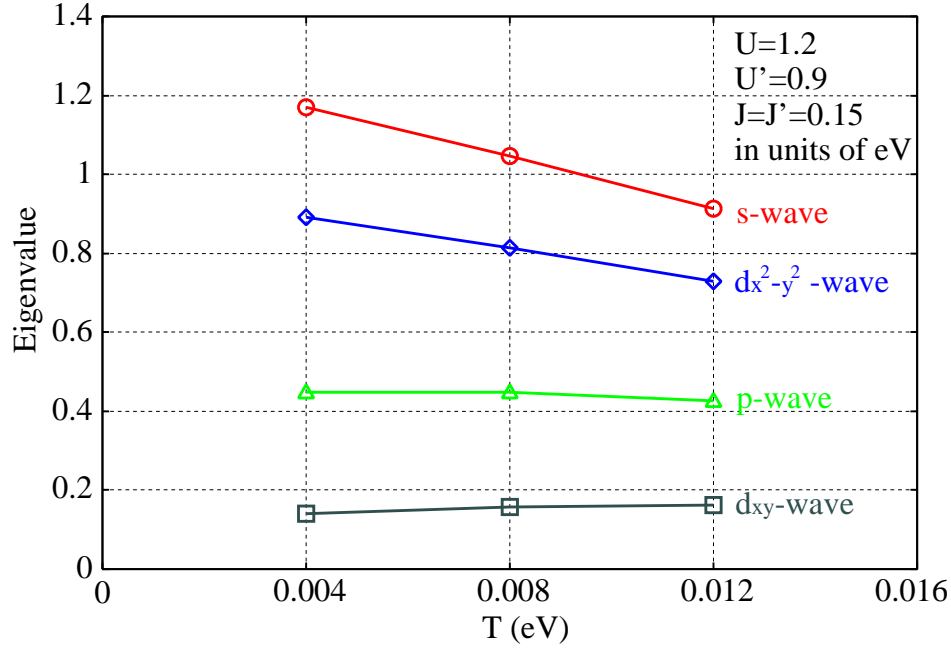
Fig. 3. (Color online) Eigenvalues of the Eliashberg equation as a function of temperature for various pairing symmetries.[50] The doping level is $x = 0.10$.

of the superconducting gap generally coincide with those of the anomalous self-energy. A remarkable feature is the sign change of the superconducting order parameter between the hole pockets (α, α' and β) and the electron pockets (γ and γ'). Thus, the pairing symmetry is not a simple s-wave, but an extended s-wave symmetry, or more specifically, an $s_{\pm}$-wave symmetry.

The superconducting order parameter on the inner hole pockets α and α' around $(0,0)$ takes nearly the same absolute value as that on the electron pockets γ and γ' around $(\pi, 0)$ and $(0, \pi)$, although the sign of the order parameter is changed between them. The absolute magnitude of the order parameter on the outer hole pocket β is about half of that on the inner hole pockets α and α'. These features are in agreement with the results of ARPES experiments.[27] Numerical calculations with finer $\boldsymbol{k}$-meshes will be necessary to investigate the detailed momentum dependence of the order parameter on each small Fermi circle.

We turn our attention to the anomalous Green's functions in the orbital representation, $F_{\ell_1 \ell_2}(k)$, which are obtained from $F_a(k)$ by eq. (25). We display only three diagonal components in the orbital representation, $F_{XZ\,XZ}(k)$, $F_{YZ\,YZ}(k)$, and $F_{X^2-Y^2\,X^2-Y^2}(k)$, at $\omega_n = \pi T$, since the other remaining diagonal elements are much smaller. Note that not all of the off-diagonal components in the orbital representation are so small, for example, $F_{XZ\,YZ}(k)$ and $F_{YZ\,XZ}(k)$ (whose plots are not shown in the present article) have magnitudes comparable to $F_{XZ\,XZ}(k)$ and $F_{YZ\,YZ}(k)$. This is due to the fact that these orbitals are well hybridized with

(a) band 2

(d) XZ orbital

(b) band 3

(e) YZ orbital
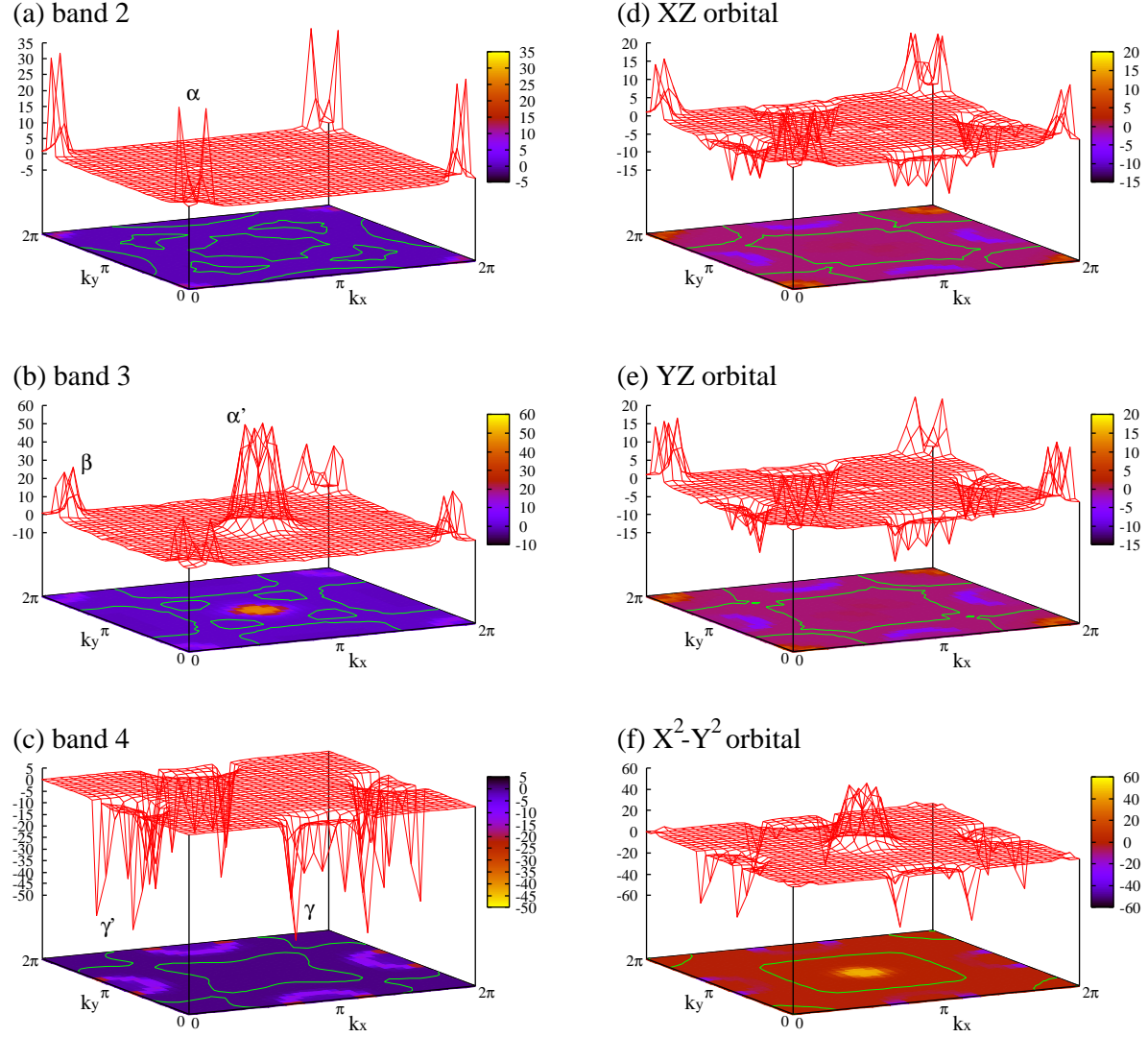
(c) band 4

(f) X²-Y² orbital

Fig. 4. (Color online) Momentum dependence of the anomalous Green's functions at $x = 0.10$ and $T = 0.008$ eV in the extended Brillouin zone. (a) $F_2(\boldsymbol{k}, \mathrm{i}\pi T)$, (b) $F_3(\boldsymbol{k}, \mathrm{i}\pi T)$, (c) $F_4(\boldsymbol{k}, \mathrm{i}\pi T)$, (d) $F_{XZ\,XZ}(\boldsymbol{k}, \mathrm{i}\pi T)$, (e) $F_{YZ\,YZ}(\boldsymbol{k}, \mathrm{i}\pi T)$, and (f) $F_{X^2-Y^2\,X^2-Y^2}(\boldsymbol{k}, \mathrm{i}\pi T)$. Note that (a)-(c) show $F_a(k)$ ($a = 2, 3, 4$) in the diagonalized-band representation, while (d)-(f) show three diagonal elements $F_{\ell\ell}(\boldsymbol{k})$ ($\ell = XZ, YZ, X^2 - Y^2$) in the orbital representation. The indices α, α', β, γ, and γ' in (a)-(c) denote the Fermi pockets shown in Fig. 2(a). The green solid lines on the base plane indicate the zero contours of the anomalous Green's functions. We find in (a)-(c) that the green lines do not cross the Fermi surfaces, i.e., there are no nodes of the superconducting order parameter on the Fermi surfaces.

each other. $F_{XZ\,X^2-Y^2}(k)$, $F_{YZ\,X^2-Y^2}(k)$, $F_{X^2-Y^2\,XZ}(k)$, and $F_{X^2-Y^2\,YZ}(k)$ (whose plots are not shown in the present article) are negligibly small. An important feature of the anomalous Green's function in the orbital representation is that, roughly speaking, the maximum and minimum of $F_{\ell\ell}(k)$ in momentum space have nearly the same absolute magnitude but
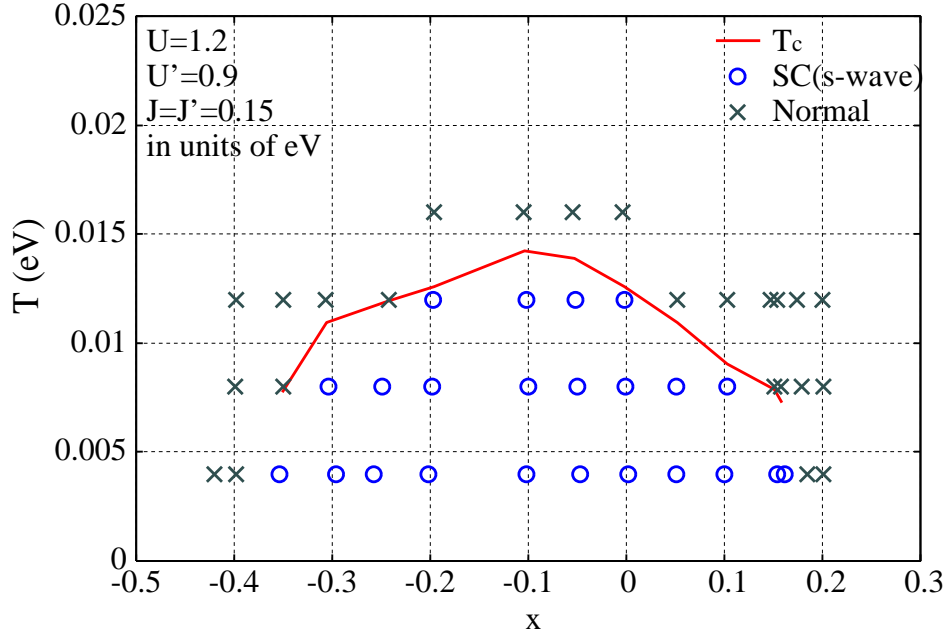
Fig. 5.   (Color online) Phase diagram. The horizontal and vertical axes denote electron doping level x and temperature (in units of eV). Negative values of x indicate hole doping. Circles (crosses) denote that the eigenvalue of the Eliashberg equation is larger (smaller) than unity, i.e, $\lambda_{\max} > 1$ ($\lambda_{\max} < 1$). In other words, the circles and crosses represent superconducting and normal states, respectively. The solid curve represents the transition temperature determined by linear interpolation. The Coulomb integrals are $U = 1.2$ eV, $U' = 0.9$ eV, and $J = J' = 0.15$ eV.

opposite signs to each other, and consequently $\sum_{\boldsymbol{k}} F_{\ell\ell}(k)$, which indicates the strength of the on-site pair correlation at orbital ℓ, is suppressed to a small value for each ℓ. We stress that this is not an accidental feature but is essential for the unconventional $s_{\pm}$-wave pairing due to electron correlations, as we shall discuss later in §5.

3.3   Doping dependence of transition temperature

Experiments suggest that carrier doping is an important method for controlling iron-pnictide superconductivity. We investigate the effects of carrier doping on the transition temperature and pairing symmetry. In the present study, we assume simply that carrier doping, which is realized by the chemical substitution of atoms in experiments, only shifts the chemical potential and retains rigidly the band structure. The dependence of the transition temperature on doping level x is displayed in Fig. 5, where the transition temperature is determined by the linear interpolation of eigenvalues. We find that the superconducting state also extends in the hole-doped region $x < 0$. Thus, our theory is consistent with the existence of superconductivity in hole-doped cases, which was suggested by some experiments. Although in practice the structural transition and SDW ordering inhibit the superconductivity near the undoped case
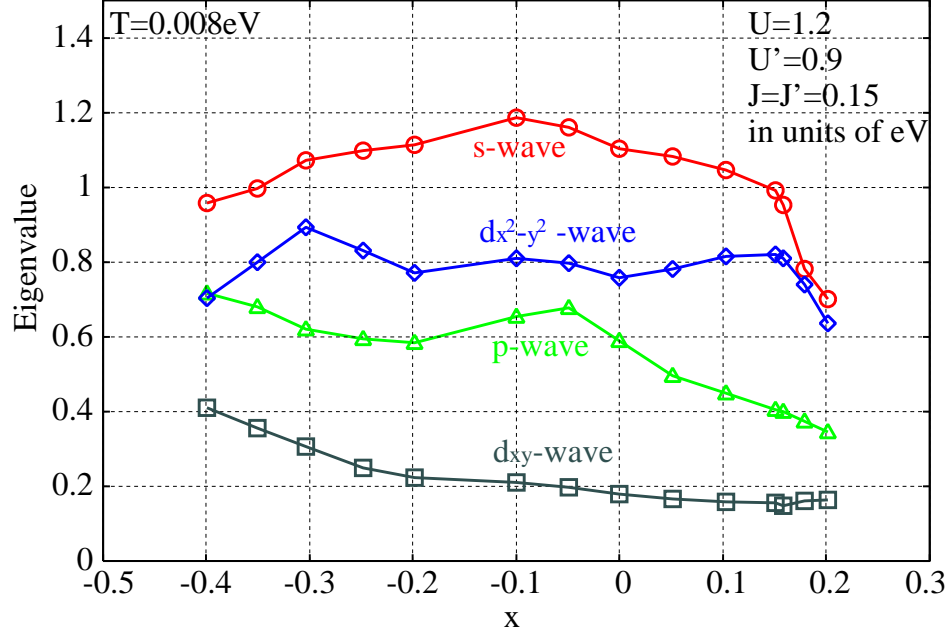
Fig. 6.   (Color online) Doping dependence of the eigenvalues of the Eliashberg equation for $U = 1.2$ eV, $U' = 0.9$ eV and $J = J' = 0.15$ eV at $T = 0.008$ eV.

$x = 0$, the structural transitions and the SDW ordering are unfortunately beyond the scope of our theory.

Concerning the pairing symmetry, the spin-singlet $s_{\pm}$-wave symmetry does not change over the whole doping region that we have calculated. The eigenvalues at $T = 0.008$ K for various symmetries are plotted in Fig. 6. The $s_{\pm}$-wave state is likely to occur robustly against other pairing symmetries in iron pnictides. Varying the doping level, the volumes of the Fermi pockets are changed, but the zero contours of the anomalous functions always avoid crossing the Fermi surfaces. Thus, the fully gapped state is realized over the whole superconducting region. Here we note that the transition temperature is suddenly suppressed at a high doping level on both sides of the electron- and hole-doping regions. This is because the hole pocket α' around (π, π) disappears near this electron-doping level and the electron pockets γ and γ' around $(\pi, 0)$ and $(0, \pi)$ disappear near this hole-doping level.

3.4   Effect of vertex corrections

It will be interesting to study the effects of the vertex corrections on the eigenvalues of the Eliashberg equation. The eigenvalues are compared for the following three cases: (i) the third-order calculation including the vertex corrections, using eq. (14), (ii) the third-order calculation without the vertex corrections, i.e., using $\Delta_{\zeta_1 \zeta_2}(k) = \Delta_{\zeta_1 \zeta_2}^{(1)}(k) + \Delta_{\zeta_1 \zeta_2}^{(2)}(k) + \Delta_{\zeta_1 \zeta_2}^{(3-1)}(k)$ instead of eq. (14), and (iii) the second-order calculation, i.e., using $\Delta_{\zeta_1 \zeta_2}(k) = \Delta_{\zeta_1 \zeta_2}^{(1)}(k) + \Delta_{\zeta_1 \zeta_2}^{(2)}(k)$ instead of eq. (14). The calculated results are displayed in Fig. 7. We see that the
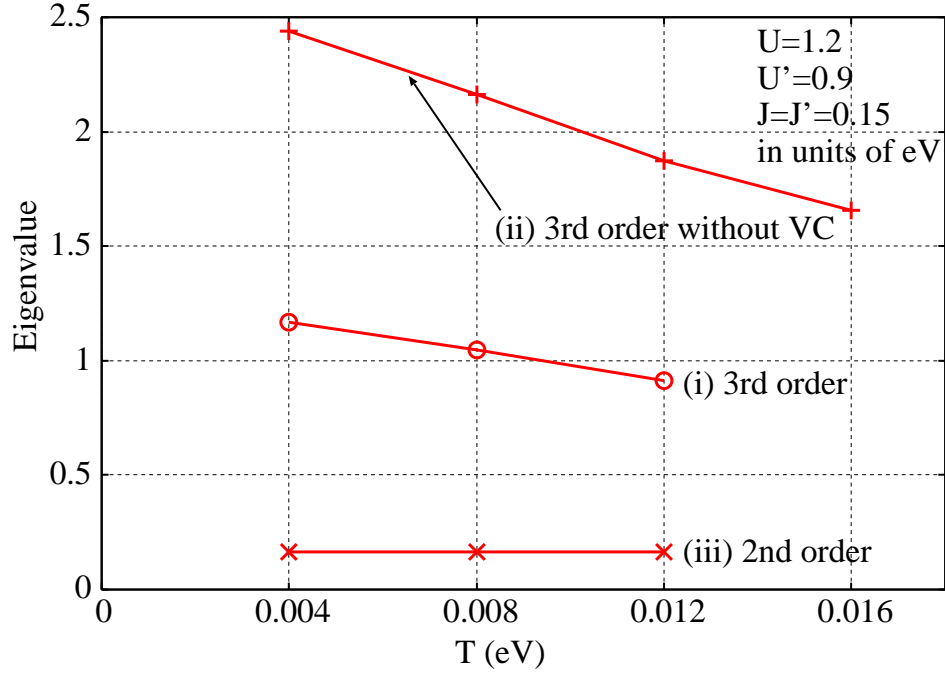
Fig. 7. (Color online) Eigenvalues of the Eliashberg equation for three cases: (i) third-order calcula-
tion (including the vertex corrections), (ii) third-order calculation without the vertex corrections,
and (iii) second-order calculation. The Coulomb integrals are $U = 1.2$ eV, $U' = 0.9$ eV and
$J = J' = 0.15$ eV.

second-order theory cannot quantitatively explain the high T_c within the realistic strength
of the Coulomb interaction, because the eigenvalues are too small. The vertex corrections
reduce the eigenvalues, and suppress the transition temperature. Thus, we consider that tran-
sition temperatures are overestimated quantitatively, when using only the terms included in
the RPA. This is qualitatively the same as in the d-wave superconductivity of single-band
systems such as cuprates and organics.[40–42] The momentum dependence of the anomalous
Green's functions $F_a(k)$ calculated without the vertex corrections (whose plots are not shown
in the present article) is almost the same as that calculated with the vertex corrections.
We consider that the vertex corrections do not affect the momentum dependence of $F_a(k)$
qualitatively, although they lower the transition temperature.

3.5 Dependence on Coulomb integrals

Eigenvalues of the Eliashberg equation for various sets of Coulomb integrals are displayed
in Table I. We find that the s-wave ($s_\pm$-wave) state is the most favorable pairing state robustly
against the other pairing states. The order of pairing strength is $s_\pm > d_{x^2-y^2} > p > d_{xy}$ for
all the cases of Coulomb integrals that we have calculated. In Table I, comparing the upper
three cases of $U = 1.2$, we speculate that eigenvalues become small for small U'. We infer from
this that processes including the interorbital Coulomb scattering U' play a role of enhancing

Table I.   Eigenvalues of the Eliashberg equation for various Coulomb integrals. $x = 0.10$ and $T = 0.004$ eV.

Coulomb integrals (eV)	s-wave	p-wave	$d_{x^2-y^2}$-wave	d_{xy}-wave
$U = 1.2,\ U' = 0.9,\ J = J' = 0.15$	1.17	0.45	0.89	0.14
$U = 1.2,\ U' = 0.6,\ J = J' = 0.3$	0.56	0.068	0.39	0.052
$U = 1.2,\ U' = 0.9,\ J = J' = 0$	1.34	0.58	1.05	0.18
$U = 1.5,\ U' = 0.5,\ J = J' = 0.5$	1.09	0.19	0.71	0.12

the eigenvalues. By comparison with the last line in Table I, we find that the eigenvalues are reduced by using a small U', but are recovered by taking slightly larger U.

4.   Analysis of 2-band Hubbard model

4.1   2-band tight-binding model by Raghu et al.

We now use another simpler model. Raghu et al. proposed a two-band model, taking account of only the xz and yz orbitals:[51]

$$E_{xz}(\boldsymbol{k}) = 2t_1 \cos k_x + 2t_2 \cos k_y + 4t_3 \cos k_x \cos k_y, \tag{28}$$

$$E_{yz}(\boldsymbol{k}) = 2t_2 \cos k_x + 2t_1 \cos k_y + 4t_3 \cos k_x \cos k_y, \tag{29}$$

$$E_{\mathrm{hyb}}(\boldsymbol{k}) = -4t_4 \sin k_x \sin k_y, \tag{30}$$

where the momentum variables k_x and k_y represent positions in the extended Brillouin zone, and the orbitals xz and yz should not be confused with the XZ and YZ orbitals in the original representation. $E_{\mathrm{hyb}}(\boldsymbol{k})$ is the hybridization term between the xz and yz bands. We take $t_1 = 0.3$, $t_2 = -0.39$, $t_3 = 0.255$, and $t_4 = -0.255$, in units of eV, which give a quantitatively realistic energy scale, specifically, a total bandwidth of about 4 eV. The chemical potential is $\mu = 0.435$ eV. The diagonalized band energies are

$$E_1(\boldsymbol{k}) = E_+(\boldsymbol{k}) - \sqrt{E_-(\boldsymbol{k})^2 + E_{\mathrm{hyb}}(\boldsymbol{k})^2}, \tag{31}$$

$$E_2(\boldsymbol{k}) = E_+(\boldsymbol{k}) + \sqrt{E_-(\boldsymbol{k})^2 + E_{\mathrm{hyb}}(\boldsymbol{k})^2}, \tag{32}$$

with

$$E_\pm(\boldsymbol{k}) = \frac{E_{xz}(\boldsymbol{k}) \pm E_{yz}(\boldsymbol{k})}{2}. \tag{33}$$

The electronic structure of this model is given in Fig. 8. The Fermi surface is qualitatively obtained from that by electronic band structure calculations and ARPES experiments, i.e., electron pockets around $(0,0)$ and (π,π) and hole pockets around $(\pi,0)$ and $(0,\pi)$. However, the energy band dispersions and the density of states are markedly different from those obtained from band calculations.
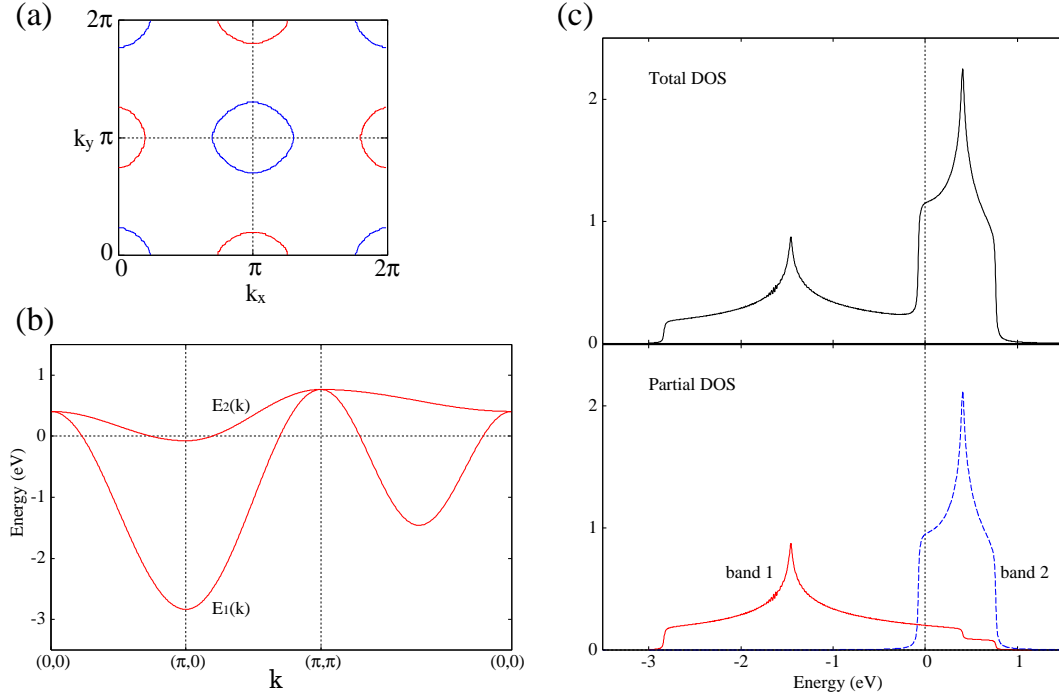
Fig. 8. (Color online) Electronic structure of the 2-band model by Raghu et al. in ref. 51. (a) Fermi surface, (b) energy band dispersion, and (c) density of states.

4.2   Eigenvalues of Eliashberg equation

For this simple 2-band model, we perform the same analysis as that for the 5-band model in §3. The calculated eigenvalues of the Eliashberg equation are presented in Fig. 9. The most favorable pairing symmetry is the odd-parity spin-triplet p-wave symmetry. This is due to the effect of the vertex corrections. As discussed in the case of Sr_2RuO_4,[43] the influence of the vertex corrections will be strong for such large particle-hole asymmetry as that in the present electronic structure. However the obtained eigenvalues are too small to explain the high T_c, and the triplet pairing state is not expected to be realized. Thus, we infer that the 2-band model is insufficient to describe the high-T_c superconductivity in iron pnictides.

5.   Discussion

We have seen in §3.2 that the eigenvalues of the Eliashberg equation for the 5-band model are sufficiently large to explain the high transition temperatures. The highest transition temperature that can be expected according to Fig. 5 is about 160 K at around $x = -0.1$, and higher than the observed highest value of 56 K. It is, of course, possible to obtain more realistic values of T_c by taking slightly smaller values of the Coulomb integrals. In the present calculations, we have not included the normal self-energy corrections in the Green's functions. If we include these corrections, then T_c is expected to be somewhat decreased owing to the effect of quasi-particle damping and mass renormalization. For a more quantitative analysis, it
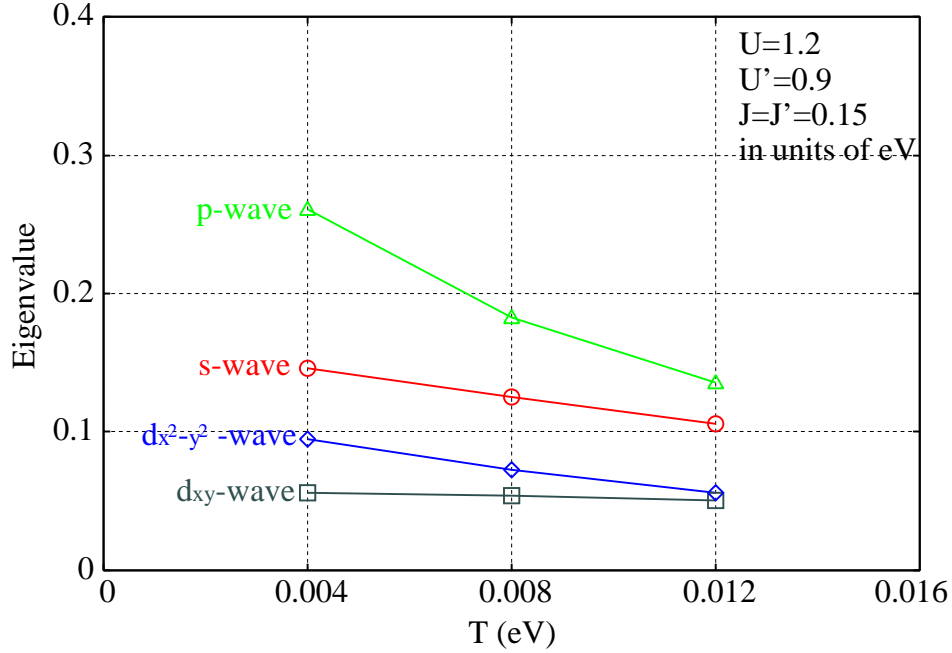
Fig. 9. (Color online) Eigenvalues of Eliashberg equation for the 2-band model as a function of temperature. The Coulomb integrals are $U = 1.2$ eV, $U' = 0.9$ eV, and $J = J' = 0.15$ eV.

is necessary to include the normal self-energy corrections. In addition, it may be necessary to use more realistic three-dimensional electronic structures, since the observed resistivity does not show such strong two-dimensionality[18, 52] as in other unconventional superconductors, such as cuprates, Sr_2RuO_4, and organics. On the other hand, the eigenvalues calculated for the 2-band model appears to be too small to explain the high T_c. The 2-band model possibly lacks some essential factors, e.g., the xy states (equivalently the $X^2 - Y^2$ states). In fact, as we have seen in the calculations using the 5-band model, the superconducting order parameter takes the maximum value on the $X^2 - Y^2$ state, and the inclusion of at least this orbital appears to be necessary to describe iron-pnictide superconductivity.

We discuss the momentum dependences of the anomalous Green's functions. As we have seen in §3.2, the anomalous function changes its sign between the hole and electron pockets. Note that this is a natural result of electron correlations. In strongly correlated electron systems, the motion of electrons is generally affected strongly by the Coulomb repulsion. Electrons move in metals, avoiding each other, in order to reduce the expectation value of the Coulomb interaction. The most significant part of the local Coulomb interaction in actual solids is the on-site intraorbital interaction, i.e., the first term of the right-hand side of eq. (4):

$$H'_U = \frac{U}{2} \sum_i \sum_\ell \sum_{\sigma \neq \sigma'} c^\dagger_{i\ell\sigma} c^\dagger_{i\ell\sigma'} c_{i\ell\sigma'} c_{i\ell\sigma}. \tag{34}$$

In superconductors, the contribution of the superconducting condensate to the expectation

value of H'_U is evaluated within a simple mean-field approximation:

$$\delta E_U = \langle H'_U \rangle \tag{35}$$

$$= \frac{U}{2} \sum_i \sum_\ell \sum_{\sigma \neq \sigma'} \langle c^\dagger_{i\ell\sigma} c^\dagger_{i\ell\sigma'} c_{i\ell\sigma'} c_{i\ell\sigma} \rangle \tag{36}$$

$$\approx \frac{U}{2N} \sum_{kk'} \sum_\ell \sum_\sigma F^\dagger_{\ell\sigma\bar\sigma}(\boldsymbol{k}) F_{\ell\bar\sigma\sigma}(\boldsymbol{k}'), \tag{37}$$

where

$$F_{\ell\bar\sigma\sigma}(\boldsymbol{k}) = \langle c_{\boldsymbol{k}\ell\bar\sigma} c_{-\boldsymbol{k}\ell\sigma} \rangle \tag{38}$$

$$F^\dagger_{\ell\sigma\bar\sigma}(\boldsymbol{k}) = \langle c^\dagger_{-\boldsymbol{k}\ell\sigma} c^\dagger_{\boldsymbol{k}\ell\bar\sigma} \rangle, \tag{39}$$

and $c_{\boldsymbol{k}\ell\sigma}$ is the Fourier transformation of $c_{i\ell\sigma}$. In odd-parity spin-triplet pairing states, δE_U vanishes completely. We now consider even-parity spin-singlet pairing states. The spin part is decoupled by $F_{\ell\sigma\sigma'}(\boldsymbol{k}) = F_\ell(\boldsymbol{k})[i\sigma_y]_{\sigma\sigma'}$ and $F^\dagger_{\ell\sigma\sigma'}(\boldsymbol{k}) = F^*_\ell(\boldsymbol{k})[-i\sigma_y]_{\sigma\sigma'}$, and the expectation value of the energy is reduced to

$$\delta E_U = \frac{U}{N} \sum_\ell \left| \sum_{\boldsymbol{k}} F_\ell(\boldsymbol{k}) \right|^2. \tag{40}$$

It will be easy to see that, in order to reduce δE_U, $|\sum_{\boldsymbol{k}} F_\ell(\boldsymbol{k})|$ should be small for each ℓ. Here note that $F_\ell(\boldsymbol{k})$ is calculated by the anomalous Green's functions:[53]

$$F_\ell(\boldsymbol{k}) = T \sum_{\omega_n} F_{\ell\ell}(k). \tag{41}$$

The momentum dependence and nodal positions of $F_{\ell\ell}(k)$ (except absolute magnitudes) are generally almost the same at all frequencies. Therefore, we may expect that the momentum dependence of $F_\ell(\boldsymbol{k})$ is approximately the same as that of $F_{\ell\ell}(k)$. As we have seen in §3.2, the maximum and minimum of $F_{\ell\ell}(k)$ in momentum space have almost the same absolute magnitude but opposite signs to each other, and consequently $\sum_{\boldsymbol{k}} F_{\ell\ell}(k)$ is suppressed to a small value for each ℓ. Thus, we find that the calculated momentum dependences of the anomalous functions $F_{\ell\ell}(k)$ are indeed such that the on-site intraorbital correlation energy δE_U is reduced. Using eqs. (25) and (27), we obtain the band representation

$$\left| \sum_{\boldsymbol{k}} F_\ell(\boldsymbol{k}) \right| = \left| \sum_{\boldsymbol{k}} \sum_a |U_{\ell a}(\boldsymbol{k})|^2 F_a(\boldsymbol{k}) \right|. \tag{42}$$

In many other unconventional superconductors including $d_{x^2-y^2}$-wave superconductors such as some heavy-fermion superconductors, this value will be suppressed by the sign change of $F_a(\boldsymbol{k})$ on each band a. On the other hand, in iron-pnictide superconductors, it is suppressed by the sign change of $F_a(\boldsymbol{k})$ not on each band but among different bands. Thus, we naturally expect that the superconducting order parameter should always take nearly the same absolute value but opposite signs between the hole pockets around the Γ point and the electron pockets around the M point, in order to reduce the correlation energy δE_U. The superconducting gap

function will also always take nearly the same absolute values between the hole pockets and the electron pockets, although the gap magnitude itself will depend on the temperature and doping level. This is expected to be confirmed by experiments, such as comprehensive ARPES studies on the band dependence of gap magnitude at various temperatures and doping levels in various iron-pnictide superconductors. If experiments indeed confirm this, they will support the realization of the $s_\pm$-wave pairing symmetry in iron-pnictide superconductors.

It will be interesting to compare our results with those of other theoretical studies. The $s_\pm$-wave or extended s-wave pairing states have been obtained by many other theoretical studies. Among them, the RPA calculations were performed by Kuroki et al. for the same 5-band Hubbard model[23] (The 5-band model used in our present study was constructed by them), and by Yanagi et al. for a more complex d-p model including the As4p orbitals explicitly.[32] We speculate that the $s_\pm$-wave pairing state will be more robustly favorable against the next most favorable pairing state, i.e., the $d_{x^2-y^2}$-wave state, in the present perturbative study than in the RPA studies. For a higher doping level $x = 0.3$ ($n = 6.3$), where the hole pocket α' around (π, π) does not exist, the $d_{x^2-y^2}$-wave state might become the most favorable as mentioned in ref. 23, but the eigenvalues will not be large enough to explain the high T_c. Our perturbative results suggest that the superconducting order parameter (and superconducting gap) does not have any nodes on the Fermi surface in the whole doping region, while nodes appear on the electron pockets around the M point in the RPA results of ref. 23, despite the fact that we have used the same model as Kuroki et al. used. The origin of this discrepancy is unclear. Other more recent RPA results by Ikeda suggest that there are not nodes on the Fermi surface.[35] Yanagi et al. suggested that the $s_\pm$-wave state is the most favorable in a d-p model with reasonable parameters, but the $d_{x^2-y^2}$-wave pairing state (the d_{XY}-wave state in the original folded Brillouin zone) becomes the most favorable, overcoming the $s_\pm$-wave state for small Hund's coupling or $J = 0$.[32] On the other hand, in our present perturbative results using the Hubbard model, we could not find any sets of Coulomb integrals for which the $d_{x^2-y^2}$-wave pairing state becomes the most favorable. We speculate that this difference originates from the difference in electronic structures used for the calculations (i.e., the 5-band Hubbard model or the more complex d-p model), rather than that in approximation methods (i.e., third-order perturbation theory or RPA). In fact, according to recent RPA results for the 5-band Hubbard model,[35] the $d_{x^2-y^2}$-wave pairing state does not overcome the $s_\pm$-wave state even for $J = 0$, as obtained from our present third-order perturbation theory. Concerning the superconducting mechanism, we consider that the magnetic fluctuations due to the Fermi surface nesting between the hole and electron pockets are an important key factor, as considered in many other theoretical studies.[23, 31–35]

We can now understand why the transition temperature drops suddenly around the high-doping regions where the hole pocket around (π, π) or the electron pocket around the M

point disappears. This can be regarded as a natural result of the $s_{\pm}$-wave pairing due to electron correlations. For the higher doping levels, the Fermi surface nesting between the hole pockets and electron pockets cannot occur, because some of the nesting Fermi surfaces disappear. In addition, the sign change of the order parameter between them can no longer occur, and enhancement of the on-site correlation energy δE_U will inevitably destabilize the $s_{\pm}$-wave pairing state. We expect that the disappearance of superconductivity at the doping levels where the hole pockets or electron pockets disappear will be observed by systematic experiments in which both the Fermi surface and transition temperatures are measured for various doping levels.

Finally, we mention that the 5-band model used in the present study is unsatisfactory regarding the following point. The volumes of the Fermi pockets appear to be quantitatively different from those of actual Fermi surfaces observed in ARPES experiments: the hole pockets have smaller volumes, while the electron pockets have larger volumes, than those in the ARPES results. This is the reason why the calculated transition temperature drops suddenly at a relatively low electron-doping level (about $x = 0.18$) and survives even up to a high hole-doping level (about $x = -0.3$), which is quantitatively inconsistent with experimental results. In actual systems, the superconductivity survives above the electron-doping level of $x = 0.18$, and vanishes at the high hole-doping level of $x = -0.3$. Thus, models possessing precise electronic structures and fermiology that are completely consistent with actual systems will be desirable for more quantitative studies.

6.   Conclusions

In the present work, we have studied the high-T_c superconductivity in iron pnictides by using multi-band Hubbard models for iron 3d electrons and by solving the Eliashberg equation within the third-order perturbation theory. The unconventional $s_{\pm}$-wave pairing symmetry is the most favorable and is highly likely to be realized, since it explains the high transition temperatures of iron pnictides. The superconducting gap is not expected to have any nodes on the Fermi surfaces in the whole doping region. This unconventional pairing symmetry is consistent with the results of many other theoretical and experimental studies. The microscopic origin of this unconventional pairing is the local Coulomb interaction among the iron 3d electrons. Thus, we can regard this high-T_c superconductivity of iron pnictides as a natural result of the electron correlation, as in the cases of other established correlation-induced (non-phonon-mediated) superconductors, such as cuprate, ruthenate, organic, and some heavy-fermion superconductors. An important difference from other unconventional superconductors is that the order parameter changes its sign not on the Fermi surface but between the Fermi pockets. We hope that further comprehensive measurements such as those mentioned in §5 will be carried out in order to confirm the realization of this intriguing pairing symmetry in iron-pnictide superconductors.

Acknowledgements

References

1) Y. Kamihara, T. Watanabe, M. Hirano, and H. Hosono: J. Am. Chem. Soc. **130** (2008) 3296.

2) Y. Kamihara, H. Hiramatsu, M. Hirano, R. Kawamura, H. Yanagi, T. Kamiya, and H. Hosono: J. Am. Chem. Soc. **128** (2006) 10012.

3) C. de la Cruz, Q. Huang, J.W. Lynn, J. Li, W. Ratcliff II, J.L. Zarestky, H.A. Mook, G.F. Chen, J.L. Luo, N.L. Wang, and P. Dai: Nature **453** (2008) 899.

4) G.F. Chen, Z. Li, D. Wu, G. Li, W.Z. Hu, J. Dong, P. Zeng, J.L. Luo, and N.L. Wang: Phys. Rev. Lett. **100** (2008) 247002.

5) Z.A. Ren, J. Yang, W. Lu, W. Yi, G.C. Che, X. L. Dong, L.L. Sun, and Z.X. Zhao: Mater. Res. Innovations **12** (2008) 105.

6) Z.A. Ren, J. Yang, W. Lu, W. Yi, X.L. Shen, Z.C. Li, G.C. Che, X.L. Dong, L.L. Sun, F. Zhou, and Z.X. Zhao: Europhys. Lett. **82** (2008) 57002.

7) X.H. Chen, T. Wu, G. Wu, R.H. Liu, H. Chen, and D.F. Fang: Nature **453** (2008) 761.

8) Z.A. Ren, W. Lu, J. Yang, W. Yi, X.L. Shen, Z.C. Li, G. C. Che, X.L. Dong, L.L. Sun, F. Zhou, Z.X. Zhao: Chin. Phys. Lett. **25** (2008) 2215.

9) H. Kito, H. Eisaki, and A. Iyo: J. Phys. Soc. Jpn. **77** (2008) 063707.

10) Z.A. Ren, G.C. Che, X.L. Dong, J. Yang, W. Lu, W. Yi, X.L. Shen, Z.C. Li, L.L. Sun, F. Zhou, and Z.X. Zhao: Europhys. Lett. **83** (2008) 17002.

11) C.H. Lee, A. Iyo, H. Eisaki, H. Kito, M.T. Fernandez-Diaz, T. Ito, K. Kihou, H. Matsuhata, M. Braden, and K. Yamada: J. Phys. Soc. Jpn. **77** (2008) 083704.

12) J. Yang, Z.C. Li, W. Lu, W. Yi, X.L. Shen, Z.A. Ren, G.C. Che, X.L. Dong, L.L. Sun, F. Zhou, and Z.X. Zhao: Supercond. Sci. Technol. **21** (2008) 082001.

13) C. Wang, L. Li, S. Chi, Z. Zhu, Z. Ren, Y. Li, Y. Wang, X. Lin, Y. Luo, S. Jiang, X. Xu, G. Cao, and Z. Xu: Europhys. Lett. **83** (2008) 67006.

14) H.H. Wen, G. Mu, L. Fang, H. Yang, and X. Zhu: Europhys. Lett. **82** (2008) 17009.

15) M. Rotter, M. Tegel, and D. Johrendt: Phys. Rev. Lett. **101** (2008) 107006.

16) J.H. Tapp, Z. Tang, B. Lv, K. Sasmal, B. Lorenz, P.C.W. Chu, and A.M. Guloy: Phys. Rev. B **78** (2008) 060505.

17) X.C. Wang, Q.Q. Liu, Y.X. Lv, W.B. Gao, L.X. Yang, R.C. Yu, F.Y. Li, and C.Q. Jin: cond-mat/0806.4688.

18) G. Wu, H. Chen, T. Wu, Y.L. Xie, Y.J. Yan, R.H. Liu, X.F. Wang, J.J. Ying, and X.H. Chen: J. Phys. Cond. **20** (2008) 422201.

19) F.C. Hsu, J.Y. Luo, K.W. Yeh, T.K. Chen, T.W. Huan, P.M. Wu, Y.C. Lee, Y.L. Huang, Y.Y. Chu, D.C. Yang, and M.K. Wu: Proc. Natl. Acad. Sci. USA **105** (2008) 14262.

20) S. Lebegue: Phys. Rev. B **75** (2007) 035110.

21) D.J. Singh, and M.H. Du: Phys. Rev. Lett. **100** (2008) 237003.

22) L. Boeri, O.V. Dolgov, and A.A. Golubov: Phys. Rev. Lett. **101** (2008) 026403.

23) K. Kuroki, S. Onari, R. Arita, H. Usui, Y. Tanaka, H. Kontani, and H. Aoki: Phys. Rev. Lett. **101** (2008) 087004.

24) S. Ishibashi, K. Terakura, and H. Hosono: J. Phys. Soc. Jpn. **77** (2008) 053709.

25) I.A. Nekrasov, Z.V. Pchelkina, and M.V. Sadovskii: Pis'ma ZhETF **88** (2008) 155.

26) F. Ma, and Z.Y. Lu: Phys. Rev. B **78** (2008) 033111.

27) H. Ding, P. Richard, K. Nakayama, K. Sugawara, T. Arakane, Y. Sekiba, A. Takayama, S. Souma, T. Sato, T. Takahashi, Z. Wang, X. Dai, Z. Fang, G.F. Chen, J.L. Luo, and N.L. Wang: Europhys. Lett. **83** (2008) 47001.

28) T. Kondo, A.F. Santander-Syro, O. Copie, C. Liu, M.E. Tillman, E.D. Mun, J. Schmalian, S.L. Bud'ko, M.A. Tanatar, P.C. Canfield, and A. Kaminski: Phys. Rev. Lett. **101** (2008) 147003.

29) C. Liu, G.D. Samolyuk, Y. Lee, N. Ni, T. Kondo, A.F. Santander-Syro, S.L. Bud'ko, J.L. McChesney, E. Rotenberg, T. Valla, A.V. Fedorov, P.C. Canfield, B.N. Harmon, and A. Kaminski: Phys. Rev. Lett. **101** (2008) 177005.

30) A.I. Coldea, J.D. Fletcher, A. Carrington, J.G. Analytis, A.F. Bangura, J.H. Chu, A.S. Erickson, I.R. Fisher, N.E. Hussey, and R.D. McDonald: Phys. Rev. Lett. **101** (2008) 216402.

31) I.I. Mazin, D.J. Singh, M.D. Johannes, and M.H. Du: Phys. Rev. Lett. **101** (2008) 057003.

32) Y. Yanagi, Y. Yamakawa, and Y. Ono: J. Phys. Soc. Jpn. **77** (2008) 123701.

33) F. Wang, H. Zhai, Y. Ran, A. Vishwanath, and D.H. Lee: cond-mat/0807.0498.

34) A.V. Chubukov, D.V. Efremov, and I. Elemin: Phys. Rev. B **78** (2008) 134512.

35) H. Ikeda: L. Phys. Soc. Jpn. **77** (2008) 123707.

36) K. Seo, B.A. Bernevig, and J. Hu: Phys. Rev. Lett. **101** (2008) 206404.

37) K. Hashimoto, T. Shibauchi, S. Kasahara, K. Ikeda, T. Kato, R. Okazaki, C.J. van der Beek, M. Konczykowski, H. Takeya, K. Hirata, T. Terashima, and Y. Matsuda: cond-mat/0810.3506.

38) A.D. Christianson, E.A. Goremychkin, R. Osborn, S. Rosenkranz, M.D. Lumsden, C.D. Malliakas, I.S. Todorov, H. Claus, D.Y. Chung, M.G. Kanatzidis, R.I. Bewley, and T. Guidi: Nature **456** (2008) 930.

39) Y. Senga, and H. Kontani: J. Phys. Soc. Jpn. **77** (2008) 113710.

40) T. Hotta: J. Phys. Soc. Jpn. **63** (1994) 4126.

41) T. Jujo, S. Koikegami, and K. Yamada: J. Phys. Soc. Jpn. **68** (1999) 1331.

42) T. Nomura, and K. Yamada: J. Phys. Soc. Jpn. **70** (2001) 2694.

43) T. Nomura, and K. Yamada: J. Phys. Soc. Jpn. **69** (2000) 3678.

44) T. Nomura, and K. Yamada: J. Phys. Soc. Jpn. **71** (2002) 1993.

45) H. Ikeda: J. Phys. Soc. Jpn. **71** (2002) 1126.

46) Y. Nisikawa, H. Ikeda, and K. Yamada: J. Phys. Soc. Jpn. **71** (2002) 1140.

47) For a review, Y. Yanase, T. Jujo, T. Nomura, H. Ikeda, T. Hotta, and K. Yamada: Phys. Reports **387** (2003) 1.

48) T. Nomura: J. Phys. Soc. Jpn. **77** (2008) Suppl. C, 123.

49) K. Nakamura, R. Arita, and M. Imada: J. Phys. Soc. Jpn. **77** (2008) 093711.

50) The eigenvalues presented here are slightly different from those in ref. 48. The present results are numerically more accurate than those in ref. 48.

51) S. Raghu, X.L. Qi, C.X. Liu, D.J. Scalapino, and S.C. Zhang: Phys. Rev. B **77** (2008) 220503.

52) X.F. Wang, T. Wu, G. Wu, H. Chen, Y.L. Xie, J.J. Ying, Y.J. Yan, R.H. Liu, and X.H. Chen: cond-mat/0806.2452.

53) For a good textbook, V.P. Mineev, and K.V. Samokhin: *Introduction to Unconventional Superconductivity* (Gordon and Breach Science Publishers, New York, 1999).